

Majorana corner modes in unconventional monolayers of the $1T$ -PtSe₂ family

Haohao Sheng,^{1,2} Yue Xie,^{1,2} Quansheng Wu,^{1,2} Hongming Weng,^{1,2}
Xi Dai,³ B. Andrei Bernevig,⁴ Zhong Fang,^{1,2} and Zhijun Wang^{1,2,*}

¹*Beijing National Laboratory for Condensed Matter Physics,
and Institute of Physics, Chinese Academy of Sciences, Beijing 100190, China*

²*University of Chinese Academy of Sciences, Beijing 100049, China*

³*Department of Physics, Hong Kong University of Science and Technology, Hong Kong 999077, China*

⁴*Department of Physics, Princeton University, Princeton, New Jersey 08544, USA*

In this work, we propose that Majorana zero modes can be realized at the corners of the two-dimensional unconventional insulator. We demonstrate that $1T$ -PtSe₂ is a symmetry indicator-free (SI-free) unconventional insulator, originating from orbital hybridization between Pt d and Se $p_{x,y}$ states. The kind of SI-free unconventionality has no symmetry eigenvalue indication. Instead, it is diagnosed directly by the Wannier charge centers by using the one-dimensional Wilson loop method. The obstructed edge states exhibit strong anisotropy and large Rashba splitting. By introducing superconducting proximity and an external magnetic field, the Majorana corner modes can be obtained in the $1T$ -PtSe₂ monolayer. In the end, we construct a two-Bernevig-Hughes-Zhang model with anisotropy to capture the Majorana physics.

I. INTRODUCTION

Majorana zero modes (MZMs) in topological superconductors [1] have attracted great interest in the past two decades and an amount of physical systems [2–7] has been proposed to realize Majorana modes. Among them, the Rashba semiconducting nanowire, which hosts Majorana end states with superconducting proximity and under a magnetic field, is a well-studied system [8, 9]. Recently, the idea of higher-order topological superconductors [10–13] broadens the research area of Majoranas and turns the Majorana modes to corners and hinges. Normally, higher-order topological superconductivity always requires either unconventional pairing order [14–20] (p -, d - or s_{\pm} -wave) or complicated junctions [21], which are difficult to implement in experiment. By using topologically protected edge states of quantum spin Hall insulators in proximity contact with an s -wave superconductor, Majorana corner modes can be realized when subjected to an external magnetic field or ordering [22, 23]. However, the obstructed edge states of unconventional insulators (obstructed atomic insulators; OAI) [24–37], viewed as a one-dimensional (1D) system exhibiting strong Rashba band splitting, also have potential to host Majorana corner modes on superconducting and magnetic substrates, which is an unexplored area (Fig. 1).

As a representative of $1T$ -phase transition metal dichalcogenides (MX_2 ; $M = \text{Ni, Pd, Pt}$; $X = \text{S, Se, Te}$), $1T$ -PtSe₂ shows many excellent characteristics, such as high electron mobility [38], helical spin texture [39], unique magnetic ordering [40], and excellent photocatalytic activity [41], etc [42–44]. Recently, the edge electronic states of PtSe₂ zigzag ribbon have been predicted theoretically [45] and subsequently confirmed experimen-

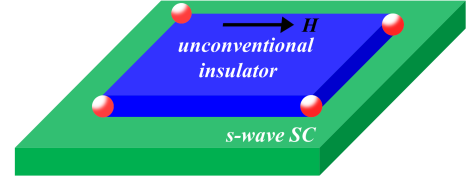


FIG. 1. (Color online) The schematic of a heterostructure composed of an unconventional insulator/OAI with Rashba edge states on top of an s -wave superconductor. Majorana corner modes can be induced under an external magnetic field.

tally [46]. The PtSe₂ ribbon is demonstrated to grow naturally along the zigzag direction, and the edge states make few-layer PtSe₂ more semimetallic [46, 47]. However, the formation mechanism of the edge states is still unrevealed.

In this work we first propose that MZMs can be realized at the corners of the unconventional $1T$ -PtSe₂ monolayer. Based on the first-principles calculations, we demonstrate that $1T$ -PtSe₂ is a symmetry indicator-free (SI-free) unconventional insulator. This kind of unconventionality is not indicated by any symmetry eigenvalues, but is directly diagnosed by the computed Wannier charge centers (WCCs). Our detailed analysis shows that the unconventional nature is attributed to the splitting of the $E@2d$ band representation (BR) of Se $p_{x,y}$ states. The obstructed edge states exhibit strong anisotropy and large Rashba splitting. By introducing superconducting proximity and an external magnetic field, the MZMs can be generated at the corners of $1T$ -PtSe₂ monolayer. The magnetic substrate CrGeTe₃ is proposed to induce a sizable gap in the Dirac edge states.

* wzj@iphy.ac.cn

II. METHODOLOGY

We carried out the first-principles calculations based on the density functional theory (DFT) with projector augmented wave (PAW) method [48, 49], as implemented in the Vienna *ab initio* simulation package (VASP) [50, 51]. The generalized gradient approximation (GGA) in the form of Perdew-Burke-Ernzerhof (PBE) function [52] was employed for the exchange-correlation potential. The kinetic energy cutoff for the plane wave expansion was set to 450 eV. The Brillouin zone was sampled by Monkhorst-Pack method in the self-consistent process, with an $18 \times 18 \times 10$ k -mesh for PtSe₂ bulk and a $10 \times 1 \times 1$ ($1 \times 6 \times 1$) k -mesh for PtSe₂ ribbon with zigzag (armchair) edge. The thickness of the vacuum was set to > 20 Å for PtSe₂ ribbon with a zigzag (armchair) edge. The irreducible representations (irreps) of electronic states were obtained from the program **IRVSP** [53]. With the obtained **tqc.data**, elementary band representations/atomic valence-electron band representations decomposition of the band structure was done on the **UnconvMat** website [25]. The maximally localized Wannier functions for the Pt d and Se p orbitals were constructed using the **WANNIER90** package [54].

III. CALCULATIONAL RESULTS

A. Electronic band structure and band representation

The 1*T*-phase PtSe₂ possesses a structure with space group $P\bar{3}m1$, where each Pt atom lies at the center of an octahedral cage formed by Se atoms, as shown in inset of Fig. 2(b). The layers are connected by van der Waals force. The Pt and Se atoms are located at the 1*a* and 2*d* Wyckoff positions, respectively. In topological quantum chemistry theory [27], the BR $\rho@q$ is induced by the ρ -irrep orbital at the q site in lattice space, which also indicates a set of k -irreps in momentum space. The generators of the BRs are elementary band representations (EBRs). Atomic valence-electron band representations (ABRs) are defined as the BRs in-

TABLE I. The atomic valence-electron band representations (ABRs) of 1*T*-PtSe₂. The Pt d orbitals form the A_{1g} , E_g , and E_g irreps at the Pt (1*a*) site, being $A_{1g}@1a$, $E_g@1a$, and $E_g@1a$ ABRs; while the Se p orbitals form the A_1 and E irreps at the Se (2*d*) site, being $A_1@2d$ and $E@2d$ ABRs.

Atom	WKS(q)	Symm. Conf.	Irreps(ρ)	ABRs($\rho@q$)
Pt	1 <i>a</i> (000)	$-3m$	$d_{z^2}:A_{1g}$	$A_{1g}@1a$
			$d_{xy,x^2-y^2}:E_g$	$E_g@1a$
			$d_{xz,yz}:E_g$	$E_g@1a$
Se	2 <i>d</i> $(\frac{1}{3}\frac{2}{3}z)(\frac{2}{3}\frac{1}{3}-z)$	$3m$	$p_z:A_1$	$A_1@2d$
			$p_{x,y}:E$	$E@2d$

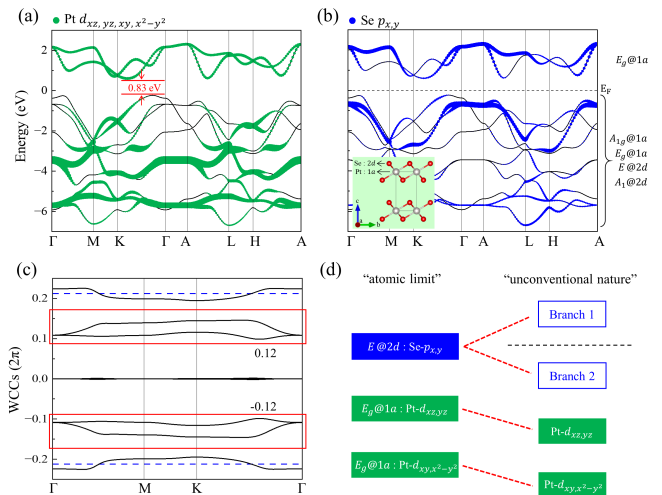


FIG. 2. (Color online) (a,b) Orbital-resolved band structures of 1*T*-PtSe₂. The sizes of (a) green and (b) blue circles represent the weights of Pt d_{xz,yz,xy,x^2-y^2} and Se $p_{x,y}$ orbitals, respectively. ABR decomposition is shown in (b). The inset of (b) presents the side view of 1*T*-PtSe₂. (c) The z -directed Wannier charge centers (WCCs) for the occupied nine bands. The blue dashed lines ($z = \pm 0.21c$) indicate the locations of the Se atoms. (d) The schematic of band hybridization, giving rise to the symmetry indicator-free (SI-free) unconventional nature. At the atomic limit (without interatom hybridization), all the bands originate from ABRs. After band hybridization in crystals, the occupied bands may form the BRs that are not located at the atoms, which is termed unconventionality. SI-free unconventionality cannot be diagnosed by BR analysis or symmetry indicator. The colors of the filled boxes indicate the atomic orbital characters, while the unfilled boxes represent the nonatomic states.

duced by the atomic valence electrons [25]. In PtSe₂, all the low energy bands originate from the valence electrons of Pt d and Se p orbitals, which form the ABRs of the compound. These ABRs are generated by **POS2ABR** and presented in TABLE I. The band structure of PtSe₂ is obtained with an indirect gap of 0.83 eV in Fig. 2(a). Based on symmetry eigenvalues (or irreps), the nine valence bands can be decomposed to the sum of ABRs: $(A_1 + E)@2d + (E_g + A_{1g})@1a$, while the two conduction bands belong to $E_g@1a$ [27, 55]. They are exactly the obtained ABRs of TABLE I. The ABRs decomposition seems consistent with the valence states of Pt⁴⁺ and Se²⁻, implying that the Se p orbitals are fully occupied and two conduction bands are mainly from the Pt d orbitals of the E_g irrep.

B. SI-free unconventional nature

On the other hand, we calculate the orbital-resolved band structures in Figs. 2(a) and 2(b). The Pt d_{xz,yz,xy,x^2-y^2} orbitals form two E_g irreps at the 1*a* site (being $E_g@1a$ ABR), while the Se $p_{x,y}$ orbitals form an

E irrep at the $2d$ site (being $E@2d$ ABR). Figure 2(a) shows most weights of the E_g -irrep Pt d orbitals below the Fermi level (E_F). In contrast, many weights of the E -irrep Se p orbitals are above the E_F in Fig. 2(b). These results are not consistent with Pt^{4+} and Se^{2-} states at all.

By using the 1D Wilson loop method [56, 57], the z -directed WCCs are computed, indicating the electronic locations along the z direction directly. The $(A_{1g} + E_g)@1a$ bands should have three WCCs at $z = 0c$, while the $(E + A_1)@2d$ bands should have WCCs at $z = \pm 0.21c$ [dashed lines in Fig. 2(c)], being aligned with Se positions. The WCCs for nine occupied bands are obtained in Fig. 2(c), and the results show that the average of the two Wilson bands in the red box is $z = 0.12c$, quite far away from the Se atoms. This indicates the unconventional nature of mismatch between the Wannier/electronic charge centers and atomic positions in PtSe_2 .

C. Origin of unconventional nature

To investigate the origin of unconventional nature, we have checked the irreps carefully, because only the bands of the same irreps can hybridize. The schematic of band hybridization in PtSe_2 is given in Fig. 2(d). Starting from the atomic limit, the energy levels of d orbitals ($E_g@1a$) are lower than that of $p_{x,y}$ orbitals ($E@2d$) in the Wannier-based tight-binding Hamiltonian extracted from the DFT calculations, giving rise to a half filling of $E@2d$ ABR at E_F . Then, the $E@2d$ ABR can be decomposed into two separate branches with branch 1 identical to $E_g@1a$, as presented in TABLE II. Due to the hybridization between Pt d ($E_g@1a$) and Se $p_{x,y}$ (branch 1 of $E@2d$), branch 1 is fully unoccupied and branch 2 is fully occupied. The hybridization process gives rise to the SI-free unconventional nature characterized by the offset charge centers, which is consistent with the obtained WCCs in the 1D Wilson loop method.

This SI-free unconventional nature is not protected by any symmetry, being of accidental obstructed atomic limit. Although it seems that the SI-free unconventional nature can be removed by changing the relative onsite energy without closing the energy gap, the substitution with

TABLE II. The k -irreps of the ABR $E@2d$ are presented below. They can be decomposed into two parts.

$E@2d$	Branch 1 (identical to $E_g@1a$)	Branch 2
$\Gamma_3^+ \oplus \Gamma_3^-$	Γ_3^+	Γ_3^-
$A_3^+ \oplus A_3^-$	A_3^+	A_3^-
$H_1 \oplus H_2 \oplus H_3$	H_3	$H_1 \oplus H_2$
$K_1 \oplus K_2 \oplus K_3$	K_3	$K_1 \oplus K_2$
$L_1^+ \oplus L_1^- \oplus L_2^+ \oplus L_2^-$	$L_1^+ \oplus L_2^+$	$L_1^- \oplus L_2^-$
$M_1^+ \oplus M_1^- \oplus M_2^+ \oplus M_2^-$	$M_1^+ \oplus M_2^+$	$M_1^- \oplus M_2^-$

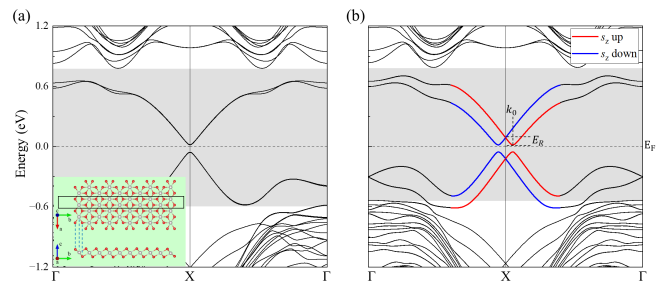


FIG. 3. (Color online) Band structures (a) without and (b) with SOC of PtSe_2 ribbon with zigzag edge. Inset of (a) presents the structure of the zigzag edge. The black rectangle represents the unit cell. Red and blue bands in (b) indicate the s_z up and s_z down channels due to SOC. The k_0 and E_R denote the momentum offset and Rashba energy, respectively.

the same group elements usually does not qualitatively change the relative onsite energy at all. As a matter of fact, all the $1T-MX_2$ compounds of the PtSe_2 family possess the SI-free unconventional nature. First, the onsite energy of M d orbitals is lower than that of X $p_{x,y}$ orbitals for all $1T-MX_2$ members at the atomic limit. Second, the interlayer hybridization of an X p_z orbital may lead to metallicity in some $1T-MX_2$ compounds [58], which does not really affect the SI-free unconventional nature (relying on the X $p_{x,y}$ orbitals). As a result, the obstructed edge states are always expected in the PtSe_2 -family compounds. Recently, the existence of SI-free unconventional nature and obstructed hinge states is demonstrated in NiTe_2 bulk, and the magnetic field filtering of hinge supercurrent in NiTe_2 -based Josephson junctions is observed experimentally [59].

D. Obstructed edge states

Due to the unconventional nature of the electronic band structure, obstructed edge states can emerge. The band structure of the zigzag edge (x direction) is presented in Fig. 3. Without spin-orbit coupling (SOC), the edge states appear in the bulk band gap (shaded area), as shown in Fig. 3(a). The obstructed edge states behave as a massive Dirac band around the X point, rather than a parabolic band, because the linear dispersion survives in a wide range ($\sim \frac{1}{3}$) of the edge Brillouin zone. The gap of the edge Dirac band is 0.07 eV. The edge gap is consistent with the previous theoretical and experimental results [45–47]. In addition, the band structure of the armchair edge (y direction) is also depicted in Fig. 6 of Appendix A. Instead of a massive Dirac band, the obstructed edge states show an M-shaped band. Moreover, the armchair edge gap is larger than the zigzag edge gap, exhibiting strong anisotropy.

Upon including SOC, the zigzag edge states will split into two massive Dirac bands, exhibiting large Rashba splitting in Fig. 3(b). The coupling strength of the Rashba SOC can be obtained as $\alpha_R = \frac{2E_R}{k_0} = 3.35$ eV

Å, where $k_0 = 0.043$ Å and $E_R = 0.072$ eV denote the momentum offset and Rashba energy, respectively. The remarkable α_R is as large as those in the BiTeI [60] and Bi/Ag(111) surface alloy [61]. As a result, two massive Dirac bands are supposed to have the opposite spin. Due to the coexistence of time reversal and M_x symmetries, $\langle s_x \rangle = 0$ is required. The x -directed magnetic field can easily lift the Kramers' degeneracy at the X point. Additionally, $\langle s_y \rangle$ and $\langle s_z \rangle$ are computed, as shown in Fig. 7 of Appendix A, which indicate that the s_z component is dominant. We conclude that the obstructed edge states exhibit large Rashba splitting and strong anisotropy. The edge atoms of ribbons are fully relaxed in the calculations. These results are obtained by the *ab initio* self-consistent calculations.

E. Proposal for MZMs in the corners

Due to the existence of obstructed edge states with large Rashba splitting and strong anisotropy, we propose that the MZMs can be realized at the corners of 1T-PtSe₂ monolayer. Under s -wave superconducting proximity and an x -directed magnetic field, the zigzag edge can be tuned to an equivalent spinless p -wave Kitaev chain [2], while the armchair edge is fully gapped (Appendix A). Thus, at the corners (ends of the zigzag edges), MZMs can be realized with a proper chemical potential. It is proposed here that MZMs exist at the corners of the two-dimensional (2D) topologically trivial insulator with unconventionality.

To simulate the Majorana corner modes in the system, we construct a 2D lattice model, consisting of two copies of Bernevig-Hughes-Zhang (BHZ) Hamiltonians,

$$\begin{aligned}
 H(\mathbf{k}) = & \{m + b(\cos k_x + \cos k_y)\}\Gamma_{0z0} \\
 & - \beta \sin k_x (\cos \theta \Gamma_{zxy} + \sin \theta \Gamma_{zxx}) \\
 & + \beta \sin k_y \Gamma_{0y0} + \xi \Gamma_{z00} - \alpha \Gamma_{xx0} + d \Gamma_{x00}.
 \end{aligned} \quad (1)$$

Here, $\Gamma_{ijk} = \rho_i \sigma_j s_k$ ($i, j, k = 0, x, y, z$). Pauli matrices ρ_i , σ_j and s_k act on BHZ, orbital, and spin spaces, respectively. ξ adds energy difference between the two copies of BHZ states. d generates the anisotropy on two different edges. α introduces the hybridization between the two copies of edge Dirac states. These parameters are estimated by fitting the band structure obtained from the first-principles calculations. In Figs. 4 (a) and 4 (b), we plot the x -directed (ZZ) and y -directed (AC) edge dispersions. In the two-BHZ model, when tuning the chemical potential μ to the degenerate states on ZZ edge, there are no Fermi-level states on the AC edge [$\mu = 0.18$ eV; the dashed line in Figs. 4 (a) and 4 (b)]. Therefore, only the ZZ edge responds to the external magnetic field $H_Z = \mu_B h_{\text{eff}} \hat{e} \cdot \mathbf{s}$ (\hat{e} is unit vector and is chosen to be $\hat{e} = e_x$ in the following) and superconducting proximity. The full Bogoliubov-de Gennes (BdG) Hamiltonian with

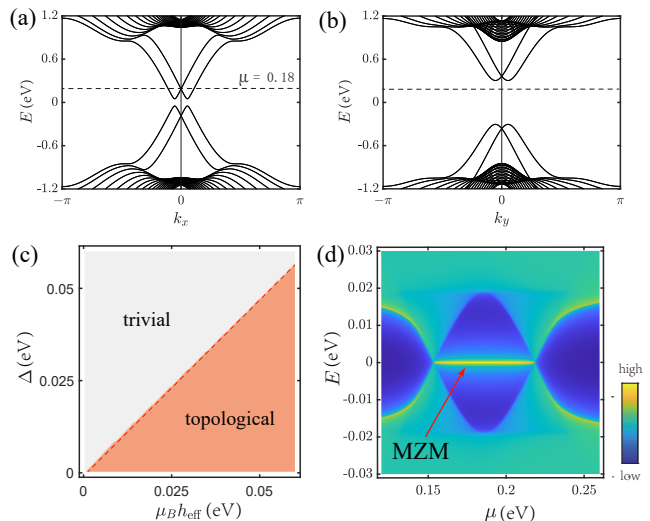


FIG. 4. (Color online) Results of the two-BHZ model. (a) Energy dispersions in a ribbon geometry along x ($L_y = 20$ lattice sites). (b) Energy dispersions in a ribbon geometry along y ($L_x = 20$ lattice sites). (c) Phase diagram with superconducting pairing (Δ) vs magnetic field (h_{eff}) with chemical potential $\mu = 0.18$ eV. The orange regime (topological) holds Majorana corner states, while the grey regime (trivial) does not. In (d), with $\mu_B h_{\text{eff}} = 0.04$ eV and $\Delta = 0.02$ eV, we plot the corner spectrum evolution as a function of μ . One can see that when tuning μ in the magnetic gap (0.15 eV $< \mu < 0.22$ eV), the MZM is obtained at the corner.

magnetism is,

$$H_{BdG}(\mathbf{k}) = \begin{pmatrix} H(\mathbf{k}) + H_Z & -i\Delta s_y \\ i\Delta^* s_y & -H^*(-\mathbf{k}) - H_Z^* \end{pmatrix}. \quad (2)$$

Both the Zeeman coupling h_{eff} and superconducting pairing order Δ can open an energy gap at μ . Specifically, they are competing with each other, giving rise to the phase diagram in Fig. 4(c). When the Zeeman gap is dominant at $k_x = 0$, the ZZ edge becomes an equivalent spinless p -wave Kitaev system. In the topological region, we demonstrate that superconducting proximity can induce MZMs as shown in Fig. 4(d), which are bounded to the corners. Very recently, based on the obstructed surface states with huge Rashba SOC in unconventional insulator Nb₃Br₈ [25, 36], 2D topological superconductivity and Majorana states are proposed to be realized in the s -wave superconductor NbSe₂/Nb₃Br₈/ferromagnetic insulator CrI₃ heterostructure [64], which is the three-dimensional version similar to our proposal.

F. Magnetic substrate CrGeTe₃

To realize the Majorana corner modes in 1T-PtSe₂ monolayer, the effective Zeeman splitting of the zigzag edge states is important; in other words, the gap due to the external magnetic field at the X point matters

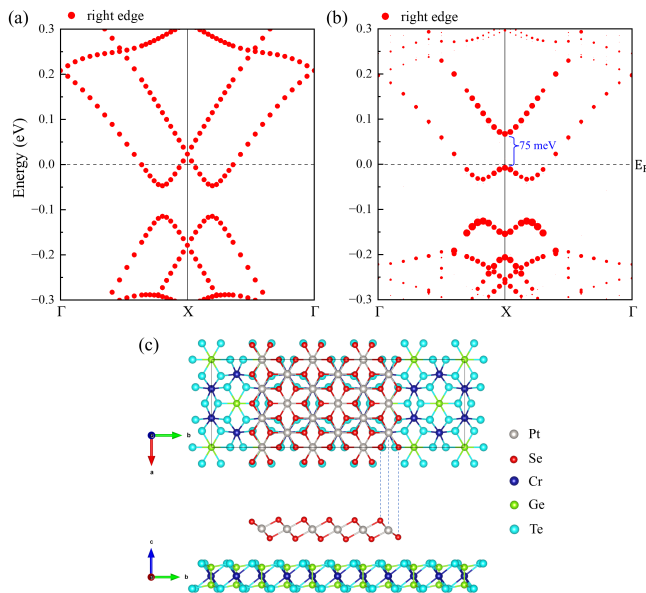


FIG. 5. (Color online) Band structures with SOC of the PtSe_2 ribbon with zigzag edge on CrGeTe_3 substrate, hosting (a) an infinite interlayer distance and (b) an actual interlayer distance obtained by relaxation. The magnetic moment of CrGeTe_3 substrate is set parallel to the x direction (along the zigzag edge direction). The size of red circle represents the weight of right edge in the PtSe_2 ribbon. The gap opened by Zeeman splitting is labeled. (c) Top and side views of the PtSe_2 ribbon with zigzag edge on CrGeTe_3 substrate. The black rectangle represents the unit cell. The right edge of the PtSe_2 ribbon is marked by dotted lines.

in this proposal. Here, we propose that the ferromagnetic insulator CrGeTe_3 [62, 63] is a proper substrate to induce a magnetic gap on the zigzag edge of $1T\text{-PtSe}_2$ monolayer. The structure for this simulation is shown in Fig. 5(c). The results of Figs. 5(a) and 5(b) show that the x -directed magnetic moment of CrGeTe_3 substrate can cause a large Zeeman gap of 75 meV at the X point. Covered by a conventional s -wave Bardeen-Cooper-Schrieffer superconductor, *e.g.* aluminum, the MZMs at the corners of $1T\text{-PtSe}_2$ monolayer are experimentally accessible.

IV. CONCLUSION

The SI-free unconventionality of charge mismatch proposed here does not have any symmetry eigenvalue indication, analog to SI-free topological insulators [55]. But it can be directly diagnosed by the computed WCCs using the 1D Wilson loop method. We demonstrate that the SI-free unconventionality is attributed to the splitting of the decomposable BR with band hybridization. The SI-free unconventionality widely exists in the compounds with $(\text{Ga}/\text{In})^{3+}$ or $(\text{Ge}/\text{Sn})^{4+}$ valence states, which suggests that the s -orbital states would be empty and all above the E_F . On the contrary, the DFT results show that these states are quite far below the E_F . The de-

tailed BR analyses and orbital-resolved band structures of SnSe_2 , CuInSe_2 , and $\text{Cu}_2\text{ZnGeSe}_4$ are presented in Appendix B. These SI-free unconventional compounds have exhibited superconductivity [65, 66], and optoelectronic or solar cell applications [67, 68].

We demonstrate that $1T\text{-PtSe}_2$ is a SI-free unconventional insulator, whose unconventional nature originates from the band hybridization between Pt d and Se $p_{x,y}$ states. The obstructed electronic states on the zigzag edge exhibit large Rashba splitting. With the high mobility and large Zeeman gap on the magnetic substrate CrGeTe_3 , the MZMs at the corners of $1T\text{-PtSe}_2$ monolayer are experimentally accessible. Additionally, our two-BHZ model is proposed to capture the Majorana corner modes in the unconventional monolayer with anisotropy. Our proposal for the Majorana corner modes in a 2D unconventional insulator/OAI can be widely studied in experiment.

Acknowledgments This work was supported by the National Natural Science Foundation of China (Grants No. 11974395, No. 12188101), the Strategic Priority Research Program of Chinese Academy of Sciences (Grant No. XDB33000000), National Key R&D Program of China (Grant No. 2022YFA1403800), and the Center for Materials Genome.

Appendix A: Band structures of PtSe_2 ribbons

The band structures with SOC of PtSe_2 ribbons with zigzag edge and armchair edge are shown in Fig. 6. The bulk band gaps (shaded area) of the two ribbons are aligned in Figs. 6(a) and 6(b). The degenerate zigzag edge states above the E_F at the X point are still located within the armchair edge gap (red line). In addition, the spin-resolved band structures of PtSe_2 ribbon with zigzag edge are presented in Fig. 7, considering SOC. We can see that $\langle s_x \rangle = 0$ and the s_z component is dominant near the E_F .

Appendix B: More examples of SI-free unconventionality

At the atomic limit (without interatom hybridization), all the states originate from ABRs. After band hybridization in crystals, the electronic charge centers of occupied bands in an insulator can not be located at any atom, which is termed as unconventional insulator/OAI. Here we show two types of unconventionality: with the symmetry indicator [SI; Fig. 8(a)] and without SI [SI-free; Fig. 8(b)]. Case (a) with an empty-site elementary band representation (EBR, generators of the BRs) has the SI [25], while case (b) cannot be diagnosed by BR analysis or symmetry indicator, termed SI-free unconventionality. The SI-free unconventionality is usually found in the compounds with $(\text{Ni}/\text{Pd}/\text{Pt})^{4+}$, $(\text{Ga}/\text{In})^{3+}$, or

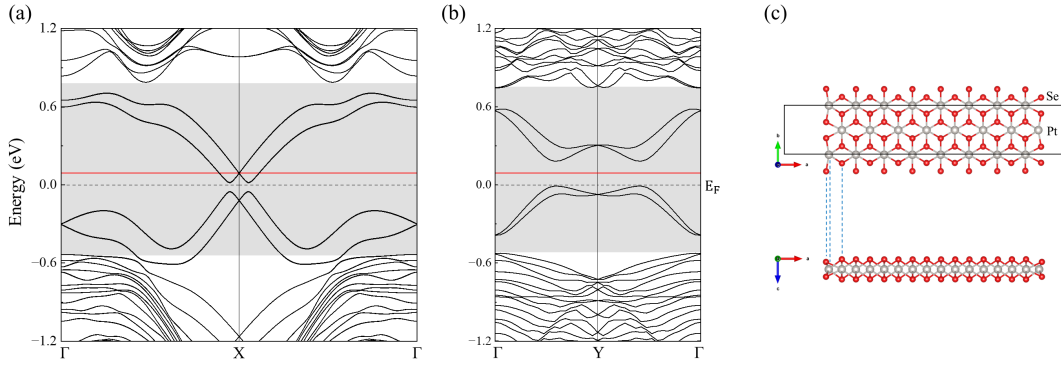


FIG. 6. (Color online) Band structures with SOC of PtSe₂ ribbons with (a) zigzag edge and (b) armchair edge. (c) Top and side views of PtSe₂ ribbon with armchair edge. The black rectangle represents the unit cell.

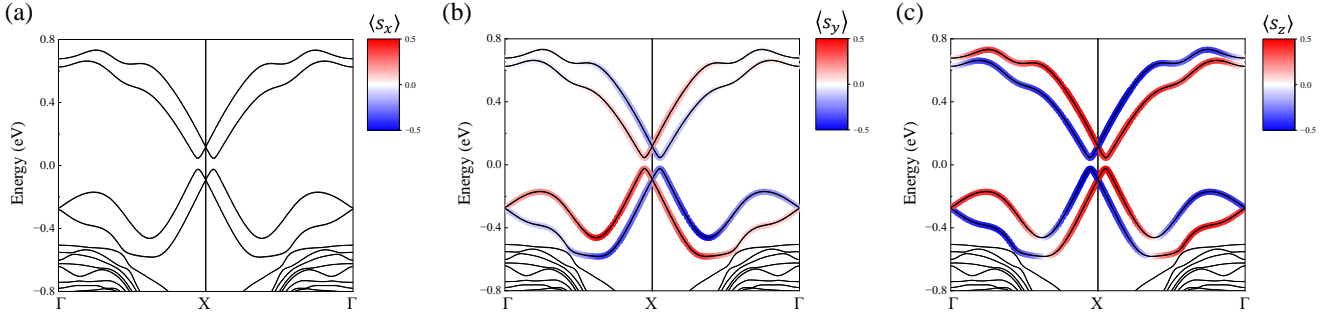


FIG. 7. (Color online) Spin-resolved band structures of PtSe₂ ribbon with zigzag edge, considering SOC. The color scales represent the expectation values of spin components (a) $\langle s_x \rangle$, (b) $\langle s_y \rangle$, and (c) $\langle s_z \rangle$.

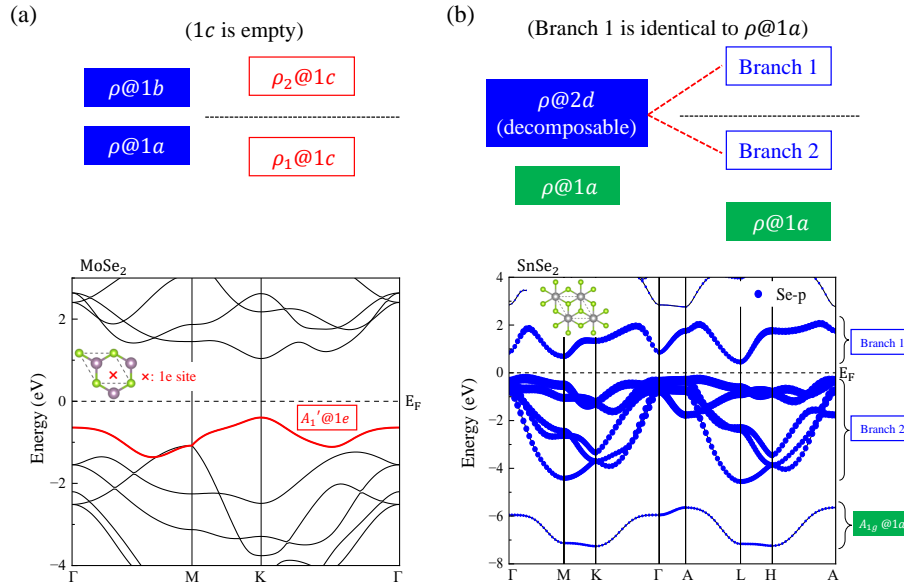


FIG. 8. (Color online) A schematic illustrating two types of the unconventionality of charge mismatch. Case (a) with an empty-site EBR has the symmetry indicator, while case (b) cannot be diagnosed by BR analysis or symmetry indicator, termed SI-free unconventionality. The colors of the filled boxes indicate the atomic orbital characters, while the unfilled boxes represent the non-atomic states.

(Ge/Sn)⁴⁺ valence states. Figure 9 presents the schematics of band hybridization and orbital-resolved band struc-

tures for SnSe₂ (space group SG $P\bar{3}m1$), CuInSe₂ (SG $I\bar{4}2d$), and Cu₂ZnGeSe₄ (SG $I\bar{4}2m$), illustrating that

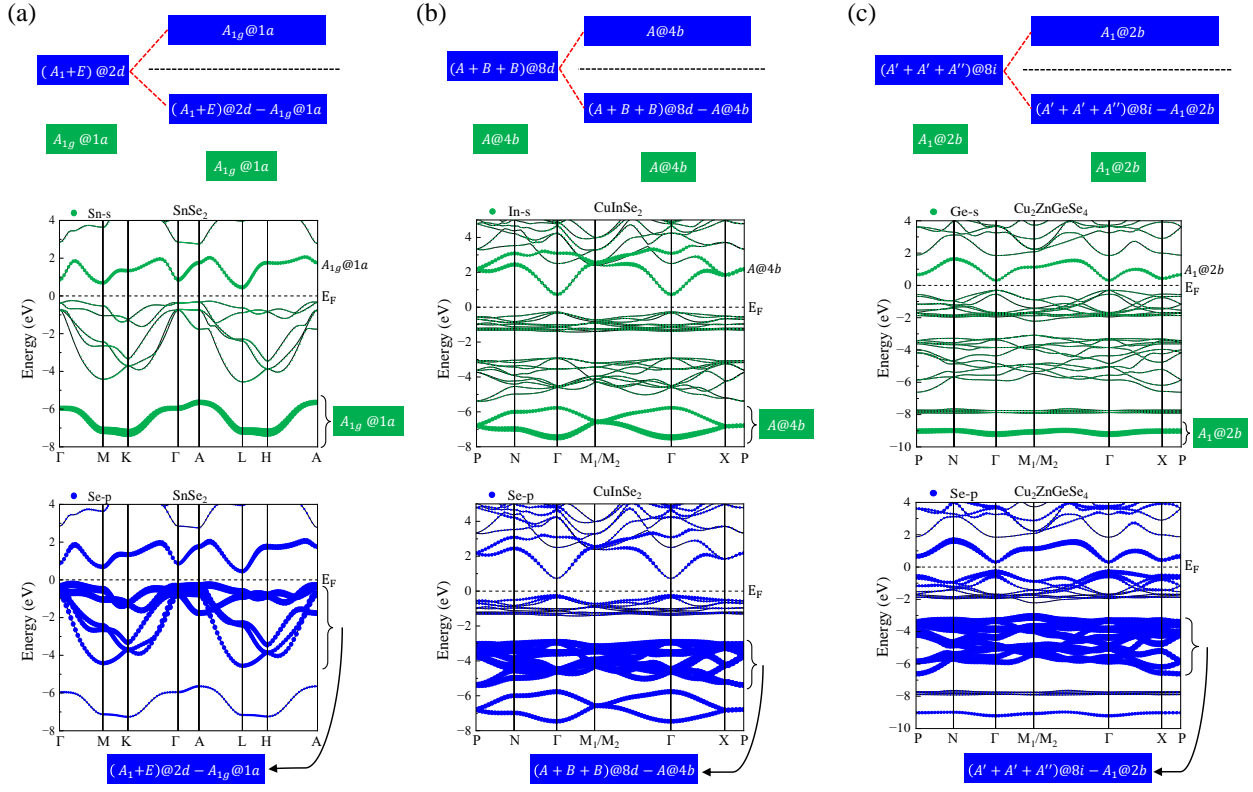


FIG. 9. (Color online) The schematics of band hybridization and orbital-resolved modified Becke-Johnson (MBJ) band structures for (a,b) SnSe_2 (space group SG $P\bar{3}m1$), (c,d) CuInSe_2 (SG $I\bar{4}2d$), and (e,f) $\text{Cu}_2\text{ZnGeSe}_4$ (SG $I\bar{4}2m$). The sizes of green and blue circles represent the weights of corresponding s and p orbitals, respectively.

their SI-free unconventional nature arises from the splitting of the decomposable BR with band hybridization.

-
- [1] J. Alicea, New directions in the pursuit of majorana fermions in solid state systems, *Reports on Progress in Physics* **75**, 076501 (2012).
- [2] A. Y. Kitaev, Unpaired majorana fermions in quantum wires, *Physics-Uspekhi* **44**, 131 (2001).
- [3] L. Fu and C. L. Kane, Superconducting proximity effect and majorana fermions at the surface of a topological insulator, *Phys. Rev. Lett.* **100**, 096407 (2008).
- [4] C.-X. Liu and B. Trauzettel, Helical dirac-majorana interferometer in a superconductor/topological insulator sandwich structure, *Phys. Rev. B* **83**, 220510 (2011).
- [5] Y. Oreg, G. Refael, and F. von Oppen, Helical liquids and majorana bound states in quantum wires, *Phys. Rev. Lett.* **105**, 177002 (2010).
- [6] R. M. Lutchyn, J. D. Sau, and S. Das Sarma, Majorana fermions and a topological phase transition in semiconductor-superconductor heterostructures, *Phys. Rev. Lett.* **105**, 077001 (2010).
- [7] S. Tewari and J. D. Sau, Topological invariants for spin-orbit coupled superconductor nanowires, *Phys. Rev. Lett.* **109**, 150408 (2012).
- [8] J. Alicea, Y. Oreg, G. Refael, F. von Oppen, and M. P. A. Fisher, Non-abelian statistics and topological quantum information processing in 1D wire networks, *Nature Physics* **7**, 412 (2011).
- [9] V. Mourik, K. Zuo, S. M. Frolov, S. R. Plissard, E. P. A. M. Bakkers, and L. P. Kouwenhoven, Signatures of majorana fermions in hybrid superconductor-semiconductor nanowire devices, *Science* **336**, 1003 (2012).
- [10] J. Langbehn, Y. Peng, L. Trifunovic, F. von Oppen, and P. W. Brouwer, Reflection-symmetric second-order topological insulators and superconductors, *Phys. Rev. Lett.* **119**, 246401 (2017).
- [11] Y. Xie, X. Wu, Z. Fang, and Z. Wang, Hybrid topological superconductivity and hinge majorana flat band in type-II dirac semimetals (2023), [arXiv:2303.11729 \[cond-mat.supr-con\]](https://arxiv.org/abs/2303.11729).
- [12] Y. Tan, Z.-H. Huang, and X.-J. Liu, Two-particle berry phase mechanism for dirac and majorana kramers pairs of corner modes, *Phys. Rev. B* **105**, L041105 (2022).
- [13] Z.-H. Huang, Y. Tan, W. Jia, L. Zhang, and X.-J. Liu, Surface chern-simons theory for third-order topological insulators and superconductors (2024),

- arXiv:2403.00316.
- [14] X. Zhu, Tunable majorana corner states in a two-dimensional second-order topological superconductor induced by magnetic fields, *Phys. Rev. B* **97**, 205134 (2018).
- [15] T. E. Pahomi, M. Sigrist, and A. A. Soluyanov, Braiding majorana corner modes in a second-order topological superconductor, *Phys. Rev. Res.* **2**, 032068 (2020).
- [16] Z. Yan, F. Song, and Z. Wang, Majorana corner modes in a high-temperature platform, *Phys. Rev. Lett.* **121**, 096803 (2018).
- [17] Q. Wang, C.-C. Liu, Y.-M. Lu, and F. Zhang, High-temperature majorana corner states, *Phys. Rev. Lett.* **121**, 186801 (2018).
- [18] T. Liu, J. J. He, and F. Nori, Majorana corner states in a two-dimensional magnetic topological insulator on a high-temperature superconductor, *Phys. Rev. B* **98**, 245413 (2018).
- [19] R.-X. Zhang, W. S. Cole, and S. Das Sarma, Helical hinge majorana modes in iron-based superconductors, *Phys. Rev. Lett.* **122**, 187001 (2019).
- [20] R.-X. Zhang and S. Das Sarma, Intrinsic time-reversal-invariant topological superconductivity in thin films of iron-based superconductors, *Phys. Rev. Lett.* **126**, 137001 (2021).
- [21] Y. Volpez, D. Loss, and J. Klinovaja, Second-order topological superconductivity in π -junction rashba layers, *Phys. Rev. Lett.* **122**, 126402 (2019).
- [22] Y.-J. Wu, J. Hou, Y.-M. Li, X.-W. Luo, X. Shi, and C. Zhang, In-plane zeeman-field-induced majorana corner and hinge modes in an s -wave superconductor heterostructure, *Phys. Rev. Lett.* **124**, 227001 (2020).
- [23] R.-X. Zhang, W. S. Cole, X. Wu, and S. Das Sarma, Higher-order topology and nodal topological superconductivity in Fe(Se,Te) heterostructures, *Phys. Rev. Lett.* **123**, 167001 (2019).
- [24] S. Nie, Y. Qian, J. Gao, Z. Fang, H. Weng, and Z. Wang, Application of topological quantum chemistry in electrides, *Phys. Rev. B* **103**, 205133 (2021).
- [25] J. Gao, Y. Qian, H. Jia, X. Guo, Z. Fang, M. Liu, H. Weng, and Z. Wang, Unconventional materials: the mismatch between electronic charge centers and atomic positions, *Science Bulletin* **67**, 598 (2022).
- [26] Y. Xu, L. Elcoro, G. Li, Z.-D. Song, N. Regnault, Q. Yang, Y. Sun, S. Parkin, C. Felser, and B. A. Bernevig, Three-dimensional real space invariants, obstructed atomic insulators and a new principle for active catalytic sites (2021), arXiv:2111.02433 [cond-mat.mtrl-sci].
- [27] B. Bradlyn, L. Elcoro, J. Cano, M. Vergniory, Z. Wang, C. Felser, M. I. Aroyo, and B. A. Bernevig, Topological quantum chemistry, *Nature* **547**, 298 (2017).
- [28] H. C. Po, H. Watanabe, and A. Vishwanath, Fragile topology and wannier obstructions, *Phys. Rev. Lett.* **121**, 126402 (2018).
- [29] Z.-D. Song, L. Elcoro, and B. A. Bernevig, Twisted bulk-boundary correspondence of fragile topology, *Science* **367**, 794 (2020).
- [30] Y. Xu, L. Elcoro, Z.-D. Song, M. G. Vergniory, C. Felser, S. S. P. Parkin, N. Regnault, J. L. Mañes, and B. A. Bernevig, Filling-enforced obstructed atomic insulators, *Phys. Rev. B* **109**, 165139 (2024).
- [31] G. Li, Y. Xu, Z. Song, Q. Yang, Y. Zhang, J. Liu, U. Gupta, V. Süß, Y. Sun, P. Sessi, S. S. P. Parkin, B. A. Bernevig, and C. Felser, Obstructed surface states as the descriptor for predicting catalytic active sites in inorganic crystalline materials, *Advanced Materials* **34**, 2201328 (2022).
- [32] D. Shao, J. Deng, H. Sheng, R. Zhang, H. Weng, Z. Fang, X.-Q. Chen, Y. Sun, and Z. Wang, Large spin hall conductivity and excellent hydrogen evolution reaction activity in unconventional PtTe_{1.75} monolayer, *Research* **6**, 0042 (2023).
- [33] R. Zhang, J. Deng, Y. Sun, Z. Fang, Z. Guo, and Z. Wang, Large shift current, π zak phase, and the unconventional nature of Se and Te, *Phys. Rev. Res.* **5**, 023142 (2023).
- [34] Y. Xu, M. G. Vergniory, D.-S. Ma, J. L. Mañes, Z.-D. Song, B. A. Bernevig, N. Regnault, and L. Elcoro, Catalog of topological phonon materials, *Science* **384**, eadf8458 (2024).
- [35] R. Zhang, H. Sheng, J. Deng, Z. Fang, Z. Yang, and Z. Wang, Unconventional phonon spectra and obstructed edge phonon modes, *Science China Physics, Mechanics & Astronomy* **67**, 246811 (2024).
- [36] H. Wu, Y. Wang, Y. Xu, P. K. Sivakumar, C. Pasco, U. Filippozzi, S. S. P. Parkin, Y.-J. Zeng, T. McQueen, and M. N. Ali, The field-free josephson diode in a van der waals heterostructure, *Nature* **604**, 653 (2022).
- [37] Z. Yang, H. Sheng, Z. Guo, R. Zhang, Q. Wu, H. Weng, Z. Fang, and Z. Wang, Superconductivity in unconventional metals, *npj Computational Materials* **10**, 25 (2024).
- [38] Y. Zhao, J. Qiao, Z. Yu, P. Yu, K. Xu, S. P. Lau, W. Zhou, Z. Liu, X. Wang, W. Ji, and Y. Chai, High-electron-mobility and air-stable 2D layered PtSe₂ fets, *Advanced Materials* **29**, 1604230 (2017).
- [39] W. Yao, E. Wang, H. Huang, K. Deng, M. Yan, K. Zhang, K. Miyamoto, T. Okuda, L. Li, Y. Wang, H. Gao, C. Liu, W. Duan, and S. Zhou, Direct observation of spin-layer locking by local rashba effect in monolayer semiconducting PtSe₂ film, *Nature Communications* **8**, 14216 (2017).
- [40] A. Avsar, C.-Y. Cheon, M. Pizzochero, M. Tripathi, A. Ciarrocchi, O. V. Yazyev, and A. Kis, Probing magnetism in atomically thin semiconducting PtSe₂, *Nature Communications* **11**, 4806 (2020).
- [41] W. Yeliang, L. Linfei, Y. Wei, S. Shiru, S. J. T., P. Jinbo, R. Xiao, L. Chen, O. Eiji, W. Yu-Qi, W. Eryin, S. Yan, Z. Y. Y., Y. Hai-tao, S. Eike F., I. Hideaki, S. Kenya, T. Masaki, C. Zhaohua, Z. Shuyun, D. Shixuan, P. Stephen J., S. T. Pantelides, and G. Hong-Jun, Monolayer PtSe₂, a new semiconducting transition-metal-dichalcogenide, epitaxially grown by direct selenization of pt, *Nano Lett.* **15**, 4013–4018 (2015).
- [42] K. Zhang, M. Yan, H. Zhang, H. Huang, M. Arita, Z. Sun, W. Duan, Y. Wu, and S. Zhou, Experimental evidence for type-II dirac semimetal in PtSe₂, *Phys. Rev. B* **96**, 125102 (2017).
- [43] X. Lin, J. C. Lu, Y. Shao, Y. Y. Zhang, X. Wu, J. B. Pan, L. Gao, S. Y. Zhu, K. Qian, Y. F. Zhang, D. L. Bao, L. F. Li, Y. Q. Wang, Z. L. Liu, J. T. Sun, T. Lei, C. Liu, J. O. Wang, K. Ibrahim, D. N. Leonard, W. Zhou, H. M. Guo, Y. L. Wang, S. X. Du, S. T. Pantelides, and H.-J. Gao, Intrinsically patterned two-dimensional materials for selective adsorption of molecules and nanoclusters, *Nature Materials* **16**, 717 (2017).
- [44] A. C. Tyner and P. Goswami, Solitons and real-space screening of bulk topology of quantum materials (2023),

- arXiv:2304.05424 [cond-mat.mtrl-sci].
- [45] S. Liu and Z. Liu, Hybridization induced metallic and magnetic edge states in noble transition-metal-dichalcogenides of PtX_2 ($X = \text{S}, \text{Se}$) nanoribbons, *Phys. Chem. Chem. Phys.* **20**, 21441 (2018).
- [46] H. Wang, Z. Liu, Y. Sun, X. Ping, J. Xu, Y. Ding, H. Hu, D. Xie, and T. Ren, Anisotropic electrical properties of aligned PtSe_2 nanoribbon arrays grown by a pre-patterned selective selenization process, *Nano Research* **15**, 4668 (2022).
- [47] R. Kempt, A. Kuc, T. Brumme, and T. Heine, Edge conductivity in PtSe_2 nanostructures, *Small Structures* **5**, 2300222 (2024).
- [48] P. E. Blöchl, Projector augmented-wave method, *Phys. Rev. B* **50**, 17953 (1994).
- [49] G. Kresse and D. Joubert, From ultrasoft pseudopotentials to the projector augmented-wave method, *Phys. Rev. B* **59**, 1758 (1999).
- [50] G. Kresse and J. Furthmüller, Efficiency of ab-initio total energy calculations for metals and semiconductors using a plane-wave basis set, *Computational Materials Science* **6**, 15 (1996).
- [51] G. Kresse and J. Furthmüller, Efficient iterative schemes for ab initio total-energy calculations using a plane-wave basis set, *Phys. Rev. B* **54**, 11169 (1996).
- [52] J. P. Perdew, K. Burke, and M. Ernzerhof, Generalized gradient approximation made simple, *Phys. Rev. Lett.* **77**, 3865 (1996).
- [53] J. Gao, Q. Wu, C. Persson, and Z. Wang, Irvsp: To obtain irreducible representations of electronic states in the vasp, *Computer Physics Communications* **261**, 107760 (2021).
- [54] N. Marzari, A. A. Mostofi, J. R. Yates, I. Souza, and D. Vanderbilt, Maximally localized wannier functions: Theory and applications, *Rev. Mod. Phys.* **84**, 1419 (2012).
- [55] H. C. Po, A. Vishwanath, and H. Watanabe, Symmetry-based indicators of band topology in the 230 space groups, *Nature Communications* **8**, 50 (2017).
- [56] B. J. Wieder, Z. Wang, J. Cano, X. Dai, L. M. Schoop, B. Bradlyn, and B. A. Bernevig, Strong and fragile topological dirac semimetals with higher-order fermi arcs, *Nature Communications* **11**, 627 (2020).
- [57] K.-S. Lin, G. Palumbo, Z. Guo, Y. Hwang, J. Blackburn, D. P. Shoemaker, F. Mahmood, Z. Wang, G. A. Fiete, B. J. Wieder, and B. Bradlyn, Spin-resolved topology and partial axion angles in three-dimensional insulators, *Nature Communications* **15**, 550 (2024).
- [58] H. Sheng, Z. Fang, and Z. Wang, Ferroelectric metals in $1\text{T}/1\text{T}'$ -phase transition metal dichalcogenide $M\text{Te}_2$ bilayers ($M = \text{Pt}, \text{Pd}, \text{and Ni}$), *Phys. Rev. B* **108**, 104109 (2023).
- [59] T. Le, R. Zhang, C. Li, R. Jiang, H. Sheng, L. Tu, X. Cao, Z. Lyu, J. Shen, G. Liu, F. Liu, Z. Wang, L. Lu, and F. Qu, Magnetic field filtering of the boundary supercurrent in unconventional metal NiTe_2 -based josephson junctions, *Nature Communications* **15**, 2785 (2024).
- [60] L. Cai, C. Yu, W. Zhao, Y. Li, H. Feng, H.-A. Zhou, L. Wang, X. Zhang, Y. Zhang, Y. Shi, J. Zhang, L. Yang, and W. Jiang, The giant spin-to-charge conversion of the layered rashba material BiTeI , *Nano Letters* **22**, 7441 (2022).
- [61] C. R. Ast, J. Henk, A. Ernst, L. Moreschini, M. C. Falub, D. Pacilé, P. Bruno, K. Kern, and M. Grioni, Giant spin splitting through surface alloying, *Phys. Rev. Lett.* **98**, 186807 (2007).
- [62] C. Gong, L. Li, Z. Li, H. Ji, A. Stern, Y. Xia, T. Cao, W. Bao, C. Wang, Y. Wang, Z. Q. Qiu, R. J. Cava, S. G. Louie, J. Xia, and X. Zhang, Discovery of intrinsic ferromagnetism in two-dimensional van der waals crystals, *Nature* **546**, 265 (2017).
- [63] X.-J. Dong, J.-Y. You, Z. Zhang, B. Gu, and G. Su, Great enhancement of Curie temperature and magnetic anisotropy in two-dimensional van der Waals magnetic semiconductor heterostructures, *Phys. Rev. B* **102**, 144443 (2020).
- [64] J. Hu, F. Yu, A. Luo, X.-H. Pan, J. Zou, X. Liu, and G. Xu, Chiral topological superconductivity in superconductor-obstructed atomic insulator-ferromagnetic insulator heterostructures, *Phys. Rev. Lett.* **132**, 036601 (2024).
- [65] E. B. Lochocki, S. Vishwanath, X. Liu, M. Dobrowolska, J. Furdyna, H. G. Xing, and K. M. Shen, Electronic structure of SnSe_2 films grown by molecular beam epitaxy, *Applied Physics Letters* **114**, 091602 (2019).
- [66] Y. Song, X. Liang, J. Guo, J. Deng, G. Gao, and X. Chen, Superconductivity in Li-intercalated 1T-SnSe_2 driven by electric field gating, *Phys. Rev. Mater.* **3**, 054804 (2019).
- [67] W. Li, Z. Pan, and X. Zhong, CuInSe_2 and $\text{CuInSe}_2\text{-ZnS}$ based high efficiency “green” quantum dot sensitized solar cells, *J. Mater. Chem. A* **3**, 1649 (2015).
- [68] L. Choubrac, M. Bär, X. Kozina, R. Félix, R. G. Wilks, G. Brammertz, S. Levchenko, L. Arzel, N. Barreau, S. Harel, M. Meuris, and B. Vermang, Sn substitution by Ge: Strategies to overcome the open-circuit voltage deficit of kesterite solar cells, *ACS Applied Energy Materials* **3**, 5830 (2020).